metals

Article

Pellet-Sintering Process for Limonitic Nickel Laterite: Effects of Operating Parameters and Performance Improvement

Gen Li [1], Deqing Zhu [1,2,*], Jian Pan [1,2], Qingshi Song [2], Wei Liu [1,2,*] and Ming Wang [3]

[1] School of Minerals Processing and Bioengineering, Central South University, Changsha 410083, China
[2] Vale-CSU Joint Laboratory for Low-Carbon and Hydrogen Metallurgy, Central South University, Changsha 410083, China; kevin.song@vale.com
[3] Quzhou Huayou Resource Recycling Technology Co., Ltd., Quzhou 324000, China
* Correspondence: dqzhu@csu.edu.cn (D.Z.); liuweicsu.edu.cn@csu.edu.cn (W.L.)

Abstract

Limonitic nickel laterite is difficult to sinter because of its high loss on ignition, high combined-water content, and complex refractory mineral composition, which often result in poor sinter strength and high solid fuel consumption. In this study, a pellet-sintering process was adopted to improve the sintering performance of limonitic nickel laterite. Pot sintering tests were carried out to investigate the effects of key process parameters—including moisture content, solid fuel dosage, return fines dosage, and drying–holding regime—on yield, tumble index, productivity index, and solid fuel consumption. The selected conditions were determined as follows: moisture content of 21%, solid fuel dosage of 5.8%, return fines dosage of 25%, drying at 450 °C for 5 min, and holding at 1000 °C for 10 min, under a fixed basicity of 1.5 and a bed height of 850 mm. Under these conditions, the yield, tumble index, productivity index, and solid fuel consumption reached 70.19%, 57.87%, 1.37 $t \cdot m^{-2} \cdot h^{-1}$, and 95.86 $kg \cdot t^{-1}$, respectively. Compared with conventional sintering, pellet sintering increased the yield, tumble index, and productivity index by 24.05%, 35.56%, and 31.73%, respectively, while reducing solid fuel consumption by 22.87%. XRD, OM, quantitative image analysis, and SEM–EDS analyses showed that pellet sintering reduced the average two-dimensional pore area fraction from 33.29% to 18.05% and the large-pore area fraction from 22.25% to 11.61%, while promoting a more continuous bonding structure characterized by a spinel-rich mineral framework, spinel–olivine eutectic-type composite bonding phases, and SFCA-type bonding phases. These results demonstrate that pellet sintering is a feasible route for improving the sintering performance and consolidation behavior of limonitic nickel laterite.

Keywords: limonitic nickel laterite; pellet sintering; operating parameters; sintering performance; tumble index; composite bonding phase

Check for updates

Academic Editor: Petros E. Tsakiridis

Received: 5 July 2026
Revised: 8 August 2026
Accepted: 17 August 2026
Published: 20 August 2026

Copyright: © 2026 by the authors. Licensee MDPI, Basel, Switzerland. This article is an open access article distributed under the terms and conditions of the Creative Commons Attribution (CC BY) license.

1. Introduction

Nickel is an important alloying element for stainless steel, superalloys, and emerging energy-storage materials. With the gradual depletion of high-grade nickel sulfide resources and the increasing demand for nickel-bearing materials, lateritic nickel ores have received increasing attention as important nickel resources [1,2]. Nickel laterites are generally classified into limonitic and saprolitic types according to their mineralogical and chemical characteristics. Compared with saprolitic laterite, limonitic nickel laterite usually contains higher Fe but lower Ni and MgO contents, and is commonly characterized by abundant

goethite, high combined-water content, and complex gangue minerals [1,3]. These characteristics make limonitic nickel laterite suitable for pyrometallurgical utilization routes such as sintering–blast furnace smelting and other Fe–Ni-bearing burden preparation processes [3,4]. Therefore, improving the sintering performance of limonitic nickel laterite is important for its efficient utilization and for the preparation of nickel-bearing sinter suitable for subsequent smelting.

However, the sintering of limonitic nickel laterite is more difficult than that of ordinary iron ores. Previous studies have shown that limonitic nickel laterite generally exhibits poor assimilability and limited liquid-phase fluidity because of its complex Fe–Cr–Mg–Al-bearing mineral phases and refractory gangue components [4,5]. Its high loss on ignition and high combined-water content consume a large amount of heat during dehydration, while moisture release and migration may deteriorate the thermal state and permeability of the sintering bed [6]. As a result, conventional sintering of limonitic nickel laterite is often associated with poor tumble strength, limited productivity, and high solid fuel consumption [4,6,7]. In addition, the formation of high-melting spinel-type phases and insufficient effective bonding phases weakens the connection between mineral particles, resulting in large pores, discontinuous bonding structures, and poor consolidation behavior [4]. Therefore, strengthening limonitic nickel laterite sintering requires the coordinated improvement of bed permeability, heat utilization, liquid-phase formation, and bonding-phase development.

Considerable efforts have been made to improve the sintering behavior of limonitic nickel laterite. Process parameters such as fuel dosage and moisture condition have been investigated to regulate the thermal state, mineral transformation, and bonding-phase formation during sintering [6,7]. Other strengthening methods, including multi-force-field co-sintering with chromite and hybrid sintering processes, have also been proposed to improve sinter quality, enhance heat utilization, and reduce fuel consumption or carbon emissions [8,9]. These studies indicate that the sintering performance of limonitic nickel laterite is jointly controlled by granulation behavior, bed permeability, thermal regulation, and the formation of effective bonding phases. In iron ore sintering, granulation is an important route for improving bed permeability because it promotes the adhesion of fine particles onto coarser nuclei, forms granules with suitable size distribution, and improves gas-flow channels in the bed [10,11]. Particle-size distribution, moisture condition, surface wettability, and granule structure strongly affect granulation behavior, bed permeability, and sintering performance [12–16]. For limonitic nickel laterite, pelletizing can improve the bed structure by forming larger and more uniform green pellets than conventional granulation. However, the effects of key pellet-sintering parameters on sintering performance and product structure remain to be systematically clarified. Therefore, it is necessary to systematically investigate the effects of key pellet-sintering parameters and evaluate the resulting performance improvement for limonitic nickel laterite.

In this study, a pellet-sintering process was adopted to improve the sintering performance of limonitic nickel laterite. Laboratory pot sintering tests were carried out to investigate the effects of key process parameters, including moisture content, solid fuel dosage, return fines dosage, and drying–holding regime, on yield, tumble index, productivity index, and solid fuel consumption. Under the selected pellet-sintering conditions, the sintering performance of pellet sintering was compared with that of conventional sintering. In addition, XRD, OM, quantitative image analysis, and SEM–EDS were used to characterize the phase composition, pore structure, phase distribution, and bonding characteristics of the product sinter. This work aims to determine suitable pellet-sintering parameters and provide microstructural evidence for the performance improvement of limonitic nickel laterite pellet sintering.

2. Materials and Methods

2.1. Raw Materials

The raw materials used in this study were obtained from a stainless-steel plant in southern China. Limonitic nickel laterite was used as the main iron-bearing raw material, while chromite concentrate, gravity dust, sintering dust, steelmaking dust, coke breeze, pulverized coal, and burnt lime were used as auxiliary raw materials. The chemical compositions of these raw materials are listed in Table 1.

Table 1. Chemical compositions of raw materials (wt.%).

Samples	TFe	Ni	Cr	SiO_2	CaO	MgO	Al_2O_3	LOI
Limonitic nickel laterite	46.08	0.77	2.74	4.52	2.18	2.08	3.50	27.78
Chromite	20.91	0.03	25.72	6.43	1.24	4.56	12.22	4.99
Gravity dust	22.83	0.41	1.67	8.26	5.15	2.96	4.08	11.75
Sintering dust	40.53	0.73	1.93	6.55	11.47	2.19	4.81	1.17
Steelmaking dust	23.76	0.46	4.88	6.12	32.78	1.74	0.25	18.22
Coke breeze	1.82	0.03	0.04	7.77	0.68	0.23	4.70	9.19
Pulverized coal	1.14	0.01	0.02	6.77	1.05	0.18	4.18	11.73
Burnt lime	0.06	–	–	0.46	85.58	0.50	0.13	–

Note: Only major components are reported. TFe, Ni, and Cr are expressed as elements, whereas the other components are reported as oxides; therefore, the totals may not equal 100 wt.%. LOI: loss on ignition of dried samples at 1000 °C in air atmosphere. The en dash (–) indicates that the corresponding value was not measured.

The limonitic nickel laterite contained 46.08 wt.% TFe, 0.77 wt.% Ni, 2.74 wt.% Cr, 4.52 wt.% SiO_2, 2.18 wt.% CaO, 2.08 wt.% MgO, 3.50 wt.% Al_2O_3, and 27.78 wt.% LOI, showing the typical compositional characteristics of limonitic nickel laterite, namely high Fe content, low Ni grade, and high combined-water content [17]. The high LOI indicates that a large amount of heat is required for water removal and mineral dehydration during pellet sintering, which may increase fuel demand and affect bed permeability and heat transfer. Therefore, moisture control and thermal pretreatment are important for the pellet sintering of limonitic nickel laterite.

Chromite concentrate served as the main Cr-bearing source in the mixture, containing 25.72 wt.% Cr, 20.91 wt.% TFe, 4.56 wt.% MgO, and 12.22 wt.% Al_2O_3. Gravity dust, sintering dust, and steelmaking dust were used as recycled iron-bearing materials. Among them, sintering dust contained 40.53 wt.% TFe and 11.47 wt.% CaO, while steelmaking dust was characterized by a high CaO content of 32.78 wt.% and an LOI of 18.22 wt.%. These recycled materials supplied Fe- and Ca-bearing components and participated in the adjustment of the overall chemical composition of the sintering mixture. Burnt lime contained 85.58 wt.% CaO and was used to adjust the binary basicity of the mixture. Coke breeze and pulverized coal were used as composite solid fuels to provide heat during limonitic nickel laterite pellet sintering.

The proximate analysis of the solid fuels used for limonitic nickel laterite pellet sintering on a dry basis is shown in Table 2. Coke breeze had a fixed carbon content of 79.43 wt.% and an ash content of 2.65 wt.%, whereas pulverized coal contained 74.57 wt.% fixed carbon and 10.21 wt.% ash. Compared with pulverized coal, coke breeze had a higher fixed carbon content and lower ash content, indicating a stronger heat-supply capacity and lower ash input during pellet sintering. In this study, pulverized coal and coke breeze were mixed at a mass ratio of 6:4 and used as composite solid fuels to regulate heat supply during the pellet sintering of limonitic nickel laterite.

Table 2. Proximate analysis of dry solid fuels (wt.%).

Sample	Fixed Carbon	Volatile	Ash
Coke breeze	79.43	17.92	2.65
Pulverized coal	74.57	15.22	10.21

Note: Moisture is excluded because the results are reported on a dry basis. Total sulfur was not measured in this study.

The particle size distributions of limonitic nickel laterite and solid fuels are shown in Table 3, while those of chromite concentrate, recycled dusts, and burnt lime are listed in Table 4. The limonitic nickel laterite showed a relatively broad particle size distribution, with 25.14 wt.% in the 1–3 mm fraction and 14.36 wt.% below 0.25 mm. This indicates that the ore contained both coarse particles and fine fractions, which could affect pellet formation and bed permeability during pellet sintering. Coke breeze and pulverized coal also showed broad size distributions, providing different combustion and heat-release characteristics during sintering.

Table 3. Particle size distributions of original limonitic nickel laterite and solid fuels (wt.%).

Size Composition, mm	>8	5–8	3–5	1–3	0.5–1	0.25–0.5	<0.25
Limonitic nickel laterite	6.65	10.05	12.52	25.14	21.28	10.00	14.36
Coke breeze	6.90	12.60	10.57	19.52	18.21	15.34	16.87
Pulverized coal	2.98	6.71	19.51	27.95	18.29	13.74	10.82

Table 4. Particle size distributions of chromite concentrate, recycled dusts and burnt lime (wt.%).

Size Composition, mm	>1	0.5–1	0.25–0.5	0.125–0.25	0.075–0.125	<0.074
Chromite	/	0.7	0.87	1.58	30.58	66.26
Gravity dust	0.49	8.56	28.01	19.92	42.51	0.51
Sintering dust	/	/	1.92	2.83	21.07	74.18
Steelmaking dust	15.77	27.53	21.99	11.91	15.49	7.31
Burnt lime	23.76	5.19	2.96	8.69	15.76	43.65

The slash (/) indicates that no material was present in the corresponding size fraction.

As shown in Table 4, chromite concentrate and sintering dust were mainly composed of fine particles, with 66.26 wt.% and 74.18 wt.% below 0.074 mm, respectively. Burnt lime also contained a high proportion of fine particles, with 43.65 wt.% below 0.074 mm, although 23.76 wt.% of particles were larger than 1 mm. These fine fractions indicate strong adhering-particle characteristics and are favorable for coating coarser particles during pellet formation. In contrast, steelmaking dust contained a relatively higher proportion of coarse particles, with 15.77 wt.% above 1 mm and 27.53 wt.% in the 0.5–1 mm fraction. Overall, the auxiliary raw materials contained sufficient fine fractions together with a certain amount of coarse particles, providing a suitable particle-size basis for particle adhesion, pellet growth, and green-pellet structure development [18].

The XRD patterns of the main raw materials are shown in Figure 1. Limonitic nickel laterite was mainly composed of goethite (FeO(OH)), quartz (SiO_2), enstatite ($MgSiO_3$), and hematite (Fe_2O_3). The presence of goethite is consistent with the high LOI of limonitic nickel laterite, indicating that a large amount of combined water would be released during heating. Quartz and enstatite were identified as the main silicate gangue phases, which may affect liquid-phase formation and bonding behavior during pellet sintering.

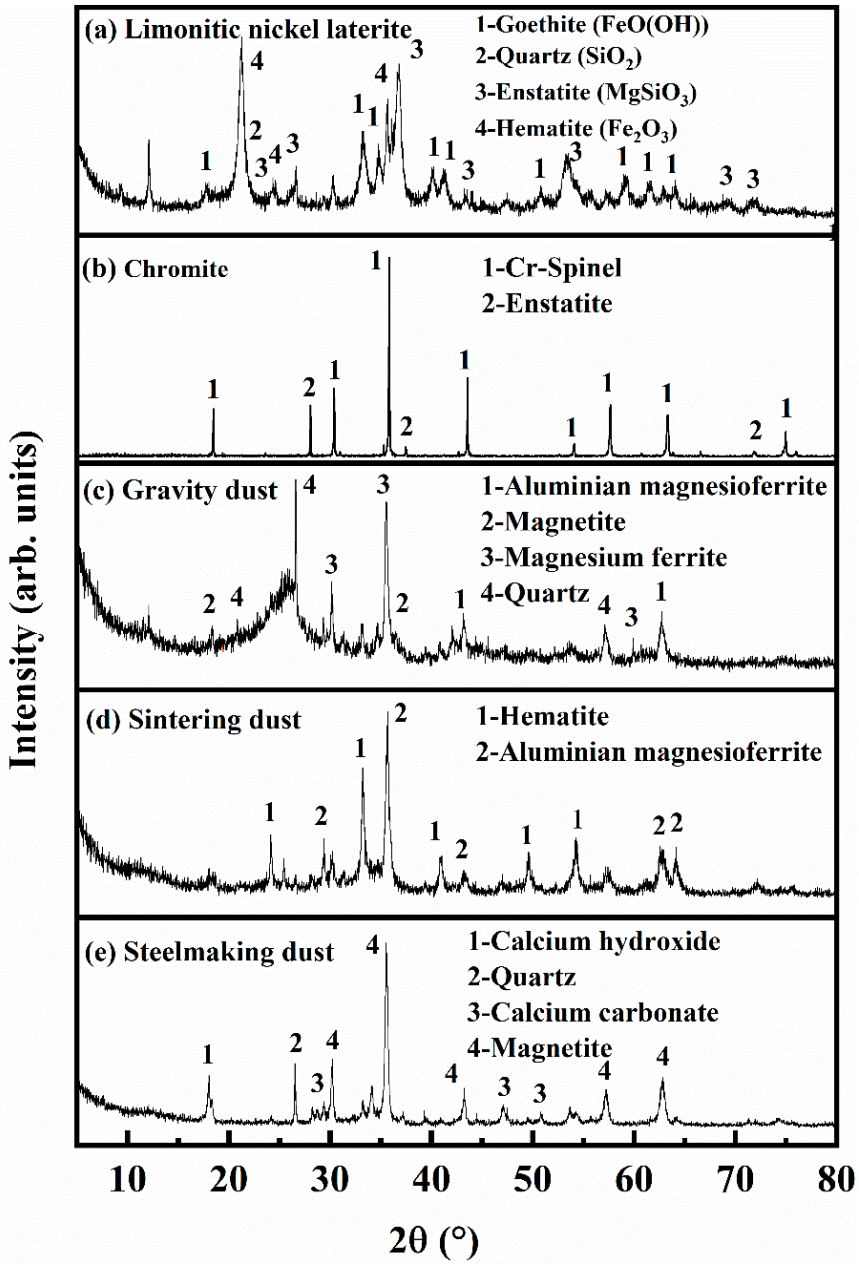


Figure 1. XRD patterns of the main raw materials: (**a**) limonitic nickel laterite, (**b**) chromite concentrate, (**c**) gravity dust, (**d**) sintering dust, and (**e**) steelmaking dust.

Chromite concentrate was mainly composed of Cr-bearing spinel and a small amount of enstatite, confirming that it served as the main Cr-bearing source in the raw material system. Gravity dust mainly consisted of aluminian magnesioferrite spinel, magnetite, magnesium ferrite, and quartz, while sintering dust was primarily composed of hematite and aluminian magnesioferrite spinel. These recycled dusts introduced Fe-bearing and spinel-type phases into the pellet-sintering mixture. Steelmaking dust was characterized by calcium hydroxide, calcium carbonate, magnetite, and a minor amount of quartz, indicating its Ca-bearing and Fe-bearing nature. The Ca-bearing phases in steelmaking dust, together with burnt lime, could contribute to basicity adjustment and affect liquid-phase formation and bonding-phase development during pellet sintering. Overall, the raw material system contained complex Fe–Cr–Mg–Al-bearing spinel phases, silicate gangue phases, and Ca-bearing components, which would influence phase transformation, liquid-phase formation, and consolidation behavior during the pellet sintering of limonitic nickel laterite.

2.2. Pelletizing and Sintering Tests

The experimental workflow for limonitic nickel laterite pellet sintering is schematically shown in Figure 2. Before pelletizing, only the limonitic nickel laterite was subjected to dry grinding until the −200 mesh fraction (<0.074 mm) accounted for 60 wt.%. Other raw materials were used without grinding. The iron-bearing raw material mixture was composed of 88 wt.% limonitic nickel laterite, 1 wt.% chromite concentrate, 5 wt.% sintering dust, 1 wt.% gravity dust, and 5 wt.% steelmaking dust. Burnt lime was added to adjust the binary basicity (CaO/SiO_2) to 1.5. Pulverized coal and coke breeze were used as composite solid fuels at a mass ratio of 6:4. This ratio was adopted from the operating practice at the source stainless-steel plant and was maintained as a fixed condition throughout the experiments to preserve the industrial relevance and comparability of the pot tests. Return fines were added according to the experimental design.

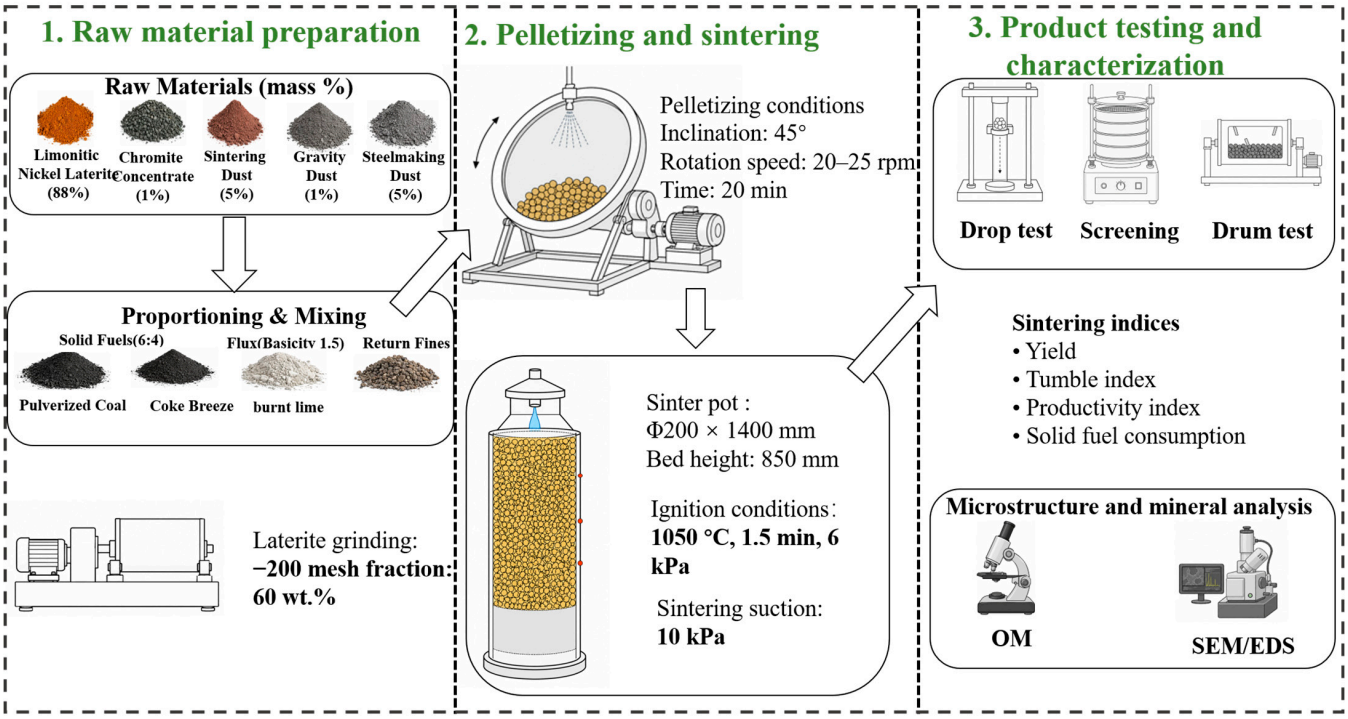


Figure 2. Schematic diagram of the experimental procedure for limonitic nickel laterite pellet sintering.

After proportioning, the raw materials, solid fuels, burnt lime, and return fines were thoroughly mixed. Tap water was added during pelletizing to adjust the mixture to the required moisture content. The same water source was used throughout all pelletizing tests. Pelletizing was conducted using a laboratory disc pelletizer (Hunan Yuke Metallurgical Technology Co., Ltd., Changsha, China) with a disc inclination of 45° and a rotation speed of 20–25 rpm. The pelletizing time was fixed at 20 min. Representative green pellets prepared under the selected pelletizing conditions were collected for physical characterization. The green-pellet size distribution was determined by screening the pellets into six size fractions: >12, 10–12, 8–10, 5–8, 3–5, and <3 mm, and the mass percentage of each fraction was calculated. For the compressive-strength test, 20 green pellets in the 10–12 mm size range were individually placed between two parallel plates of a universal testing machine and compressed until fracture. The maximum load at fracture was recorded, and the average compressive strength was reported in $N \cdot pellet^{-1}$. Drop strength was determined by repeatedly dropping individual green pellets from a height of 0.5 m onto a steel plate. The test was terminated when fracture occurred or when the number of drops reached 20. Pellets remaining intact after 20 drops were recorded as having a drop strength of

≥20 drops·pellet^{-1}. The obtained wet green pellets were then charged into the sinter pot for subsequent drying, holding, ignition, and sintering.

Pot sintering tests were performed in a laboratory sinter pot with an inner diameter of 200 mm and a height of 1400 mm. The bed height was fixed at 850 mm in accordance with the actual operating bed height at the stainless-steel plant, and 1.0 kg of hearth-layer material was placed at the bottom of the pot. Pre-ignition drying and post-ignition holding were carried out inside the sinter pot, and the corresponding temperature and time were adjusted according to the experimental design. Ignition was conducted at 1050 °C for 1.5 min under a suction pressure of 6 kPa. After ignition, sintering was performed under a suction pressure of 10 kPa. The sintering endpoint was determined when the flue gas temperature reached its maximum value and then began to decrease.

After sintering, the sintered product was cooled, subjected to drop testing, and then screened. The product sinter and return fines were weighed separately for calculating the sintering indices. For microstructural characterization, three representative pieces were selected from each of the conventional-sintering and pellet-sintering products. One polished section was prepared from each piece, and at least five randomly selected fields on each section were examined by optical microscopy. Representative regions were subsequently analyzed by SEM–EDS. The remaining product sinter was further subjected to drum testing.

2.3. Experimental Design and Evaluation Indices

To investigate the effects of key process parameters on the pellet-sintering performance of limonitic nickel laterite, a series of single-factor pot sintering tests were carried out. The investigated variables included moisture content, solid fuel dosage, return fines dosage, and drying–holding regime. The drying–holding regime consisted of pre-ignition drying temperature, pre-ignition drying time, post-ignition holding temperature, and post-ignition holding time. In each group of tests, only one process parameter was changed, while the other operating conditions were kept constant. The investigated levels were 19–22% for moisture content, 5–6.5% for solid fuel dosage, 10–30% for return fines dosage, 350–500 °C for drying temperature, 1–7 min for drying time, 800–1100 °C for holding temperature, and 6–12 min for holding time. The fixed conditions for each test series are specified in the corresponding figure captions. The binary basicity, bed height, pulverized-coal-to-coke-breeze mass ratio, pelletizing time, ignition conditions, and sintering suction were maintained at 1.5, 850 mm, 6:4, 20 min, 1050 °C for 1.5 min under 6 kPa, and 10 kPa, respectively. A single-factor experimental design was employed to evaluate the individual effects of the investigated parameters and identify suitable operating ranges. The tests on moisture content, solid fuel dosage, and return fines dosage were independently repeated three times at each investigated level, and the results are reported as mean ± standard deviation. The drying and holding conditions were evaluated through screening tests, with one pot test conducted at each investigated level.

The pellet-sintering performance was evaluated using yield, tumble index, productivity index, and solid fuel consumption. The yield was calculated according to Equation (1):

$$Y = \frac{M_p}{M_p + R_{out}} \times 100 \quad (1)$$

where Y is the yield of product sinter (%), M_p is the mass of product sinter after screening (kg), and R_{out} is the mass of return fines generated after drop testing and screening (kg).

The tumble strength of the product sinter was evaluated according to ISO 3271:2015 [19]. After drum testing, the sample was screened using a 6.3 mm sieve. The tumble index was

used to evaluate the tumble strength of the product sinter and was calculated according to Equation (2):

$$TI = \frac{m_{+6.3}}{m_0} \times 100 \quad (2)$$

where TI is the tumble index (%), m_0 is the mass of the sample before drum testing (kg), and $m_{+6.3}$ is the mass retained above 6.3 mm after drum testing (kg).

The productivity index was calculated according to Equation (3):

$$P = \frac{M_p}{t \cdot S} \quad (3)$$

where P is the productivity index ($t \cdot m^{-2} \cdot h^{-1}$), M_p is the mass of product sinter (t), t is the sintering time (h), and S is the cross-sectional area of the sinter pot (m^2).

The solid fuel consumption was calculated according to Equation (4):

$$SFC = \frac{m_{fuel,dry}}{M_p} \quad (4)$$

where SFC is the solid fuel consumption ($kg \cdot t^{-1}$), $m_{fuel,dry}$ is the dry mass of solid fuel charged into the sintering mixture (kg), and M_p is the mass of product sinter (t). The calculation boundary included only the solid fuel charged into the sintering mixture; external energy inputs associated with grinding, pelletizing, pre-ignition drying, and post-ignition holding were not included. Therefore, the reported reduction refers specifically to solid fuel consumption rather than total process energy consumption. These four indices were used to evaluate the effects of process parameters on yield, tumble index, productivity index, and solid fuel consumption.

2.4. Characterization Methods

The chemical compositions of the raw materials were determined by X-ray fluorescence spectroscopy (XRF; Axios mAX, PANalytical B.V., Almelo, The Netherlands). The loss on ignition (LOI) was measured by heating the samples to constant mass and calculating the mass loss. The proximate analysis of coke breeze and pulverized coal was conducted to determine the fixed carbon, volatile matter, and ash contents. The particle size distributions of the raw materials were determined by dry sieving using standard sieves.

The mineral compositions of the main raw materials were identified by X-ray diffraction (XRD; RIGAKU D/Max 2500, Rigaku Corporation, Akishima, Tokyo, Japan) using Cu Kα radiation over a 2θ range of 10–80°. Representative samples of the conventional sinter and pellet sinter were also analyzed under the same XRD conditions. Representative sintered samples were mounted, sectioned, ground, and polished for microstructural observation. The polished sections were observed using reflected-light optical microscopy (OM; Leica DM4500P, Leica Microsystems GmbH, Wetzlar, Germany), and selected regions were further characterized by scanning electron microscopy equipped with energy-dispersive X-ray spectroscopy (SEM–EDS; FEI Quanta 200, FEI Company, Hillsboro, OR, USA). EDS elemental mapping of Fe, Ca, Al, and Si was further performed in the same fields of view as the SEM observations of the conventional sinter and pellet sinter. The pore structures of the conventional sinter and pellet sinter were semi-quantitatively analyzed from reflected-light optical micrographs using Image-Pro Plus 6.0. Multiple representative fields were selected from the polished sections at the same magnification. The pore area fraction was calculated as the percentage of the analyzed image area occupied by open pores and resin-filled voids. Pores with an equivalent diameter greater than 50 μm were classified as large pores, and the corresponding large-pore area fraction was calculated separately.

3. Results and Discussion

3.1. Effect of Moisture Content on Pellet-Sintering Performance

The effect of moisture content on the pellet-sintering performance of limonitic nickel laterite is shown in Figure 3, with the other operating conditions kept constant. With increasing moisture content from 19% to 21%, the tumble index increased from 43.5% to 57.87%, and the productivity index increased from 0.82 to 1.37 $t \cdot m^{-2} \cdot h^{-1}$. When the moisture content further increased to 22%, the tumble index and productivity index slightly decreased to 56.61% and 1.31 $t \cdot m^{-2} \cdot h^{-1}$, respectively. Although the yield reached its maximum at 20% and the solid fuel consumption was relatively low at this moisture level, the overall performance was more favorable at 21% because of the higher tumble strength and sintering productivity.

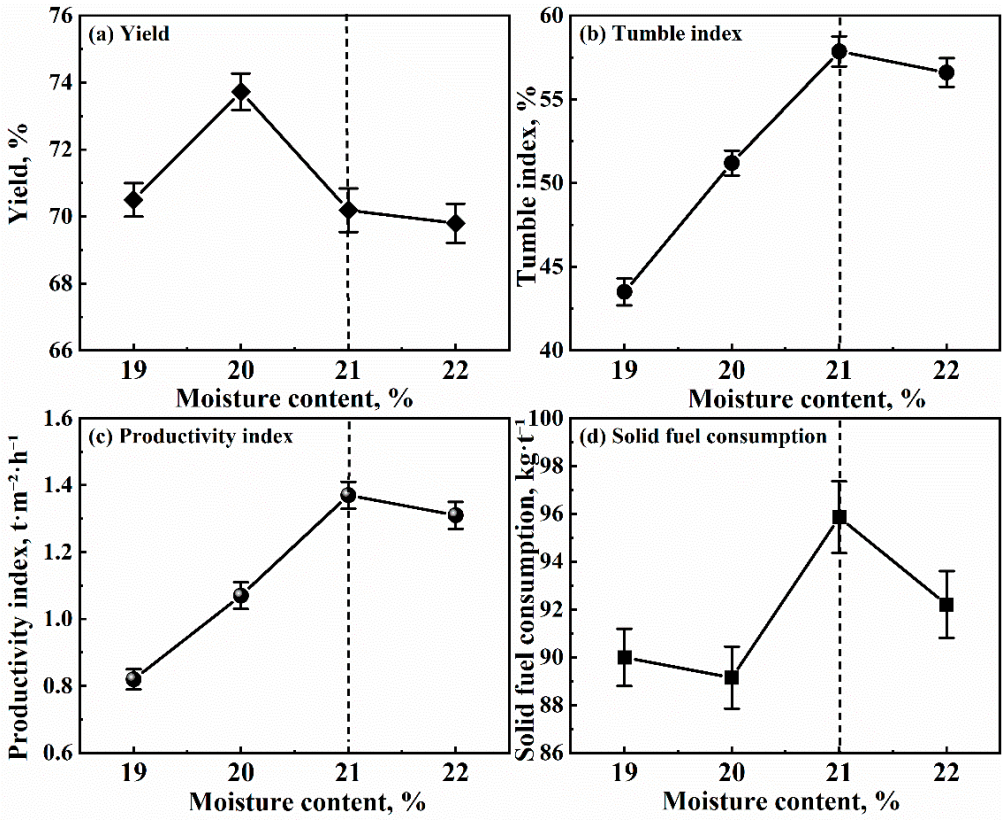


Figure 3. Effect of moisture content on the pellet-sintering performance of limonitic nickel laterite: (**a**) yield, (**b**) tumble index, (**c**) productivity index, and (**d**) solid fuel consumption. The dashed line indicates the selected moisture content of 21%. Error bars represent the standard deviations of three independent pot tests (n = 3). The solid fuel dosage, return fines dosage, drying conditions, and holding conditions were fixed at 5.8%, 25%, 450 °C for 5 min, and 1000 °C for 10 min, respectively.

The influence of moisture is mainly associated with granulation quality and bed permeability. Within a suitable range, water forms liquid bridges between fine particles, promotes the adhesion of adhering fines onto nuclei, and improves the strength and size uniformity of wet green pellets [20,21]. This helps maintain inter-pellet voids and gas-flow channels, thereby improving bed permeability and accelerating the downward movement of the combustion front. Insufficient moisture weakens particle adhesion and increases loose fines, resulting in poor permeability and slower sintering. Excessive moisture increases the heat demand for evaporation and promotes moisture migration and condensation in the lower bed, which may enlarge the over-wet zone and reduce effective heat utilization. Therefore, 21% was selected as the suitable moisture content for subsequent pellet-sintering tests.

3.2. Effect of Solid Fuel Dosage on Pellet-Sintering Performance

The effect of solid fuel dosage on the pellet-sintering performance of limonitic nickel laterite is shown in Figure 4, with the other operating conditions kept unchanged. As the solid fuel dosage increased from 5% to 6.5%, the yield increased continuously from 60.46% to 73.07%, indicating that increasing fuel addition promoted sinter consolidation and reduced the generation of return fines. The tumble index remained at a relatively high level between 5.5% and 5.8%, reaching 58.07% and 57.87%, respectively. The productivity index increased from 1.23 to 1.37 $t \cdot m^{-2} \cdot h^{-1}$ when the fuel dosage increased from 5% to 5.8%, but decreased sharply to 1.01 $t \cdot m^{-2} \cdot h^{-1}$ at 6.5%. Meanwhile, the solid fuel consumption first decreased from 101.8 to 93.09 $kg \cdot t^{-1}$, and then increased to 102.48 $kg \cdot t^{-1}$ at 6.5%. Therefore, although the highest yield was obtained at 6.5%, the overall sintering performance was more favorable at 5.8% because of its higher productivity index, relatively high tumble index, and acceptable fuel consumption.

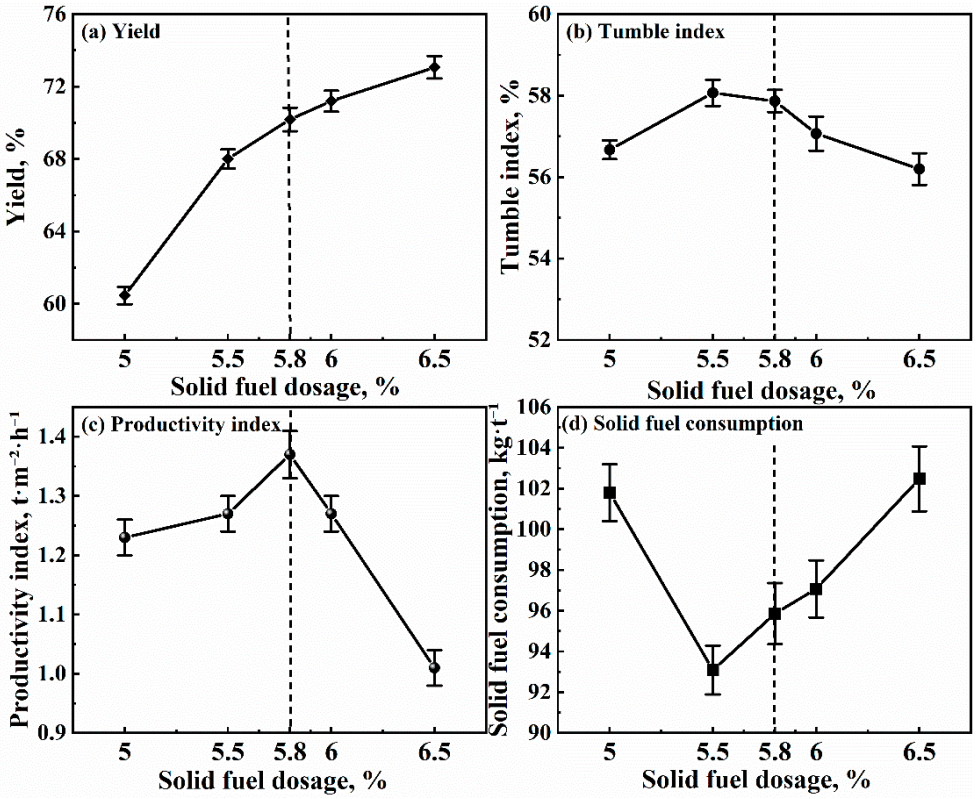


Figure 4. Effect of solid fuel dosage on the pellet-sintering performance of limonitic nickel laterite: (**a**) yield, (**b**) tumble index, (**c**) productivity index, and (**d**) solid fuel consumption. The dashed line indicates the selected solid fuel dosage of 5.8%. Error bars represent the standard deviations of three independent pot tests (n = 3). The moisture content, return fines dosage, drying conditions, and holding conditions were fixed at 21%, 25%, 450 °C for 5 min, and 1000 °C for 10 min, respectively.

The influence of solid fuel dosage is mainly associated with heat supply, combustion-zone evolution, and liquid-phase formation during sintering [22]. Insufficient fuel cannot provide enough heat for dehydration, mineral transformation, and bonding-phase formation, resulting in weak consolidation, low yield, and high return fines generation. Increasing the fuel dosage within a suitable range raises the thermal level of the bed and promotes liquid-phase formation, which strengthens particle bonding and improves tumble strength and productivity. However, excessive fuel may broaden the high-temperature zone, intensify over-melting, and increase gas-flow resistance in the bed. This can slow the downward movement of the combustion front and reduce sintering productivity. In addition, excessive

fuel addition directly increases fuel input and may reduce effective heat utilization, leading to higher solid fuel consumption. Therefore, a solid fuel dosage of 5.8% was selected for subsequent pellet-sintering tests.

3.3. Effect of Return Fines Dosage on Pellet-Sintering Performance

The effect of return fines dosage on the pellet-sintering performance of limonitic nickel laterite is shown in Figure 5, with the other operating conditions kept constant. When the return fines dosage increased from 10% to 20%, the yield increased from 67.23% to 72.01%, and the tumble index increased from 55.27% to 59.07%. Further increasing the return fines dosage to 25% decreased the yield and tumble index to 70.19% and 57.87%, respectively, whereas the productivity index reached its maximum value of 1.37 $t \cdot m^{-2} \cdot h^{-1}$. At 30% return fines dosage, the solid fuel consumption further decreased to 92.52 $kg \cdot t^{-1}$, but the yield and productivity index decreased to 67.55% and 1.21 $t \cdot m^{-2} \cdot h^{-1}$, respectively. Therefore, the suitable return fines dosage was considered to be in the range of 20–25%. Although the 20% return fines dosage gave higher yield and tumble index, 25% was selected considering its higher productivity index and lower solid fuel consumption.

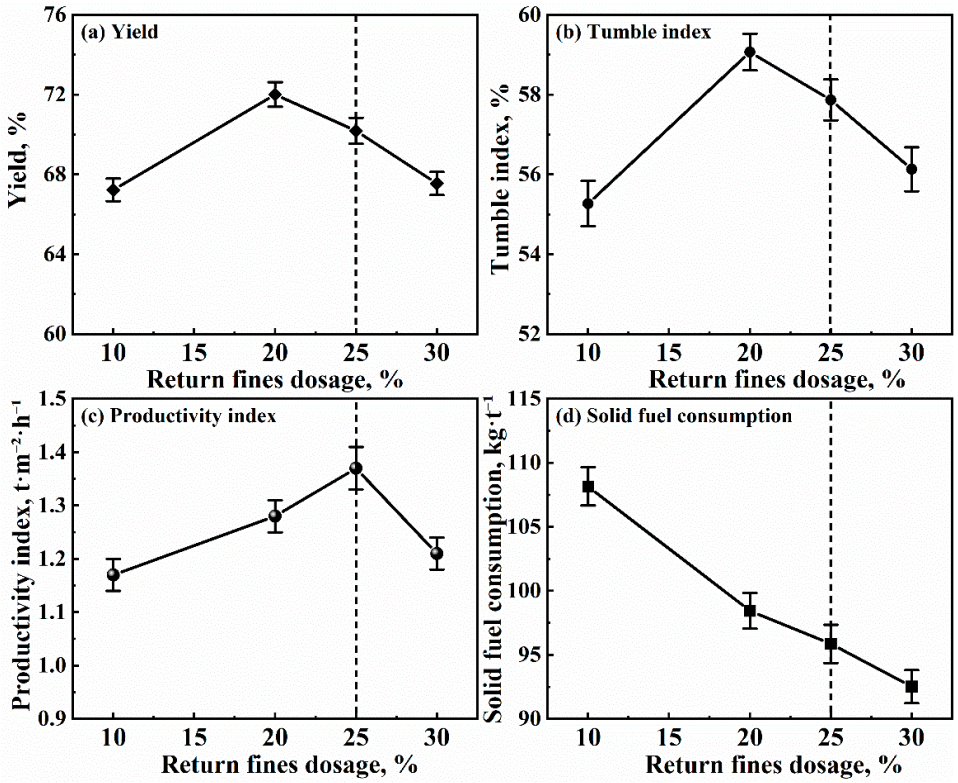


Figure 5. Effect of return fines dosage on the pellet-sintering performance of limonitic nickel laterite: (**a**) yield, (**b**) tumble index, (**c**) productivity index, and (**d**) solid fuel consumption. The dashed line indicates the selected return fines dosage of 25%. Error bars represent the standard deviations of three independent pot tests (n = 3). The moisture content, solid fuel dosage, drying conditions, and holding conditions were fixed at 21%, 5.8%, 450 °C for 5 min, and 1000 °C for 10 min, respectively.

The influence of return fines dosage is mainly related to granulation behavior, bed permeability, and return-fines circulation [23]. At a low return fines dosage, the lack of suitable nuclei weakens granule formation and leads to a higher proportion of loose fine particles, which increases gas-flow resistance and lowers the yield. Increasing return fines within a suitable range improves the particle-size distribution of the mixture and provides nuclei for pellet growth, thereby forming a more permeable pellet bed and promoting the downward movement of the combustion front. However, excessive return fines increase

the circulating load and reduce the effective proportion of newly added raw materials in the sintering bed. In addition, excessive recycled particles may weaken the uniformity of green pellets and disturb stable consolidation during sintering. Therefore, a return fines dosage of 25% was selected for subsequent pellet-sintering tests.

3.4. Effect of Drying–Holding Regime on Pellet-Sintering Performance

The drying–holding regime was divided into pre-ignition drying and post-ignition holding. The effects of drying temperature, drying time, holding temperature, and holding time on the pellet-sintering performance of limonitic nickel laterite are shown in Figures 6 and 7. During each group of tests, only one drying or holding parameter was changed, while the other operating conditions were kept constant.

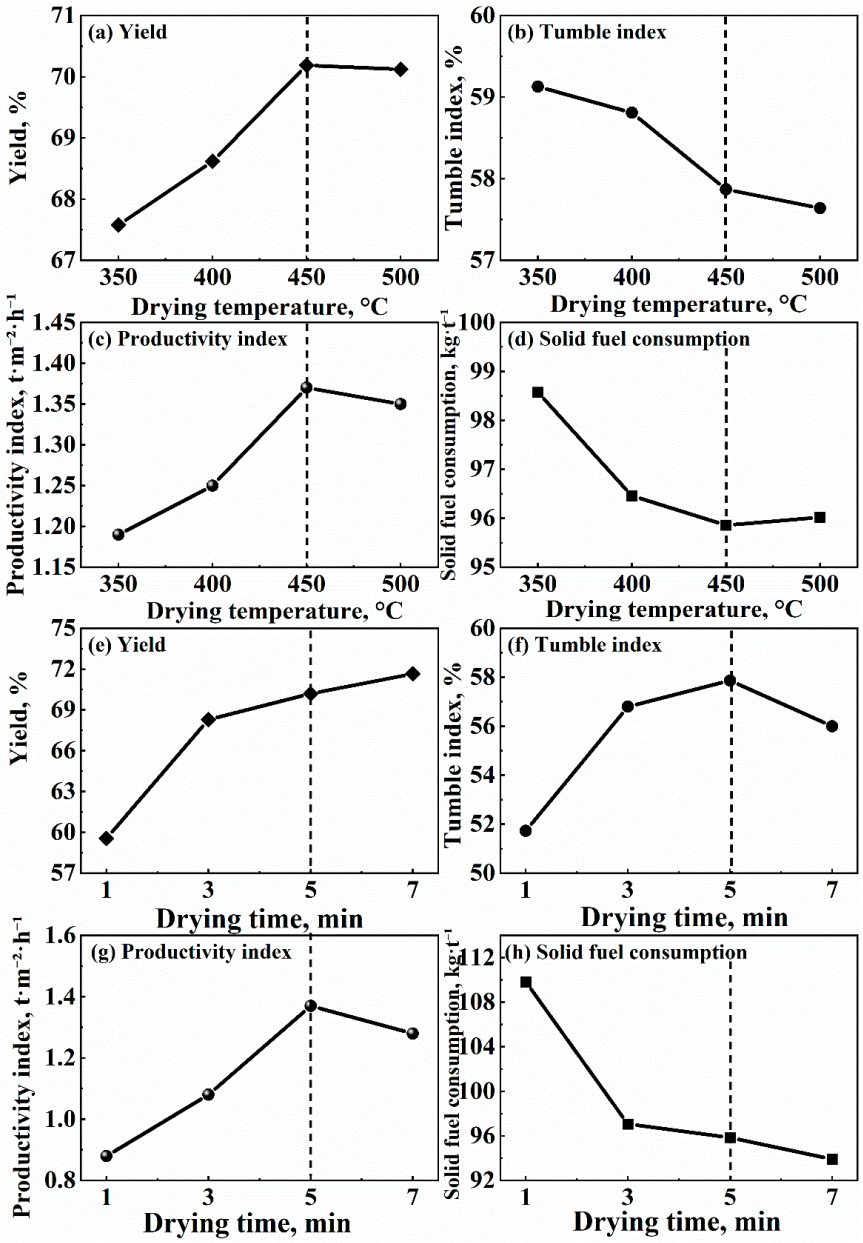


Figure 6. Effect of drying regime on the pellet-sintering performance of limonitic nickel laterite: (**a**–**d**) drying temperature and (**e**–**h**) drying time. The dashed lines indicate the selected drying temperature of 450 °C and drying time of 5 min. The moisture content, solid fuel dosage, return fines dosage, and holding conditions were fixed at 21%, 5.8%, 25%, and 1000 °C for 10 min, respectively; drying time and temperature were fixed at 5 min and 450 °C in the corresponding test series.

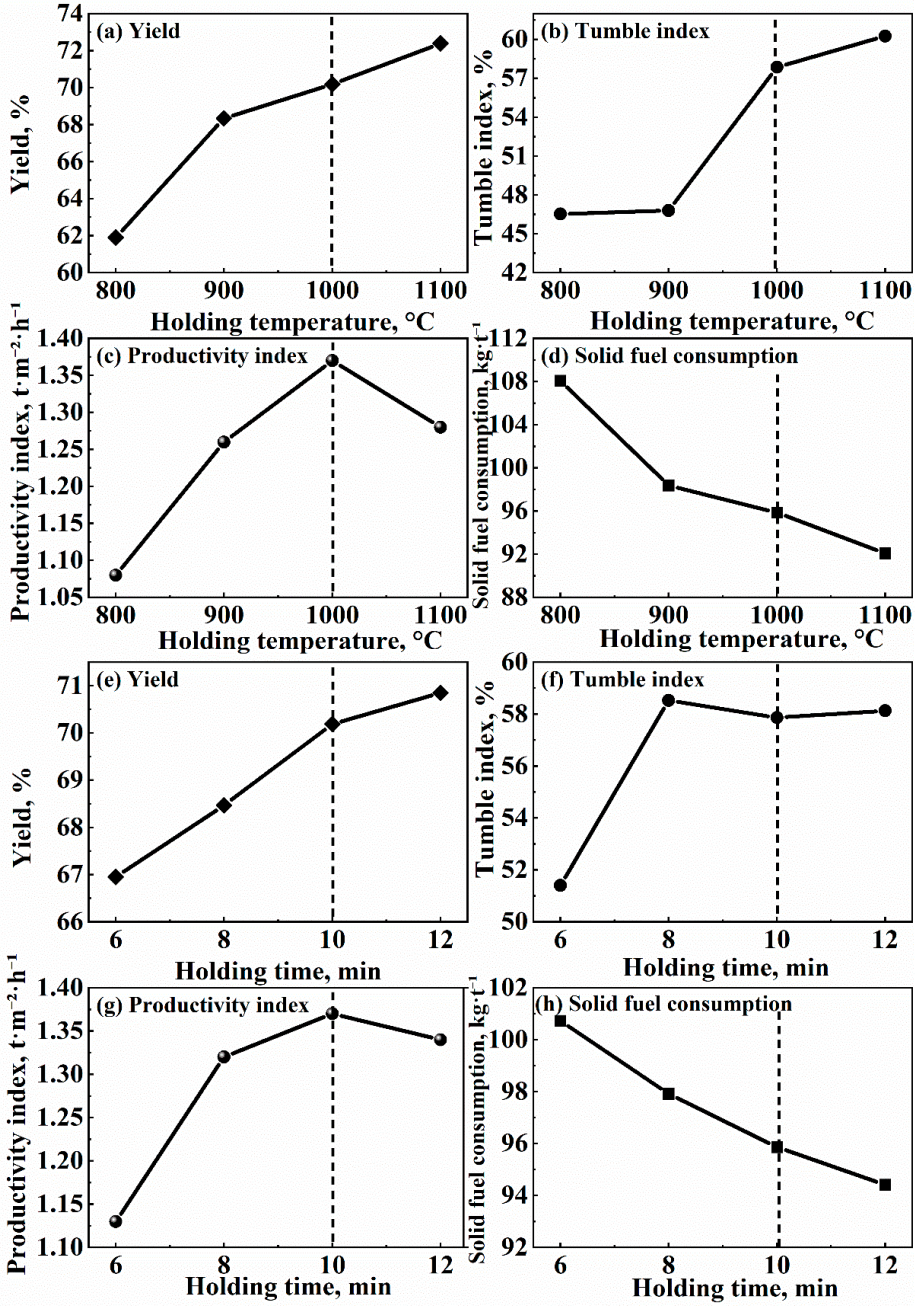


Figure 7. Effect of holding regime on the pellet-sintering performance of limonitic nickel laterite: (**a**–**d**) holding temperature and (**e**–**h**) holding time. The dashed lines indicate the selected holding temperature of 1000 °C and holding time of 10 min. The moisture content, solid fuel dosage, return fines dosage, and drying conditions were fixed at 21%, 5.8%, 25%, and 450 °C for 5 min, respectively; the holding time was fixed at 10 min in the temperature series, and the holding temperature at 1000 °C in the time series.

For the drying regime, as shown in Figure 6, increasing the drying temperature from 350 °C to 450 °C increased the yield from 67.58% to 70.19%, and the productivity index increased from 1.19 to 1.37 $t \cdot m^{-2} \cdot h^{-1}$. Meanwhile, the solid fuel consumption decreased from 98.57 to 95.86 $kg \cdot t^{-1}$. Further increasing the drying temperature to 500 °C slightly decreased the yield and productivity index to 70.12% and 1.35 $t \cdot m^{-2} \cdot h^{-1}$, respectively. The tumble index showed a slight decreasing tendency with increasing drying temperature, decreasing from 59.13% at 350 °C to 57.64% at 500 °C. Overall, 450 °C gave the highest yield and productivity index, while maintaining a relatively low solid fuel consumption.

The drying time also affected the pellet-sintering performance. When the drying time increased from 1 min to 5 min, the yield increased from 59.55% to 70.19%, the tumble index increased from 51.73% to 57.87%, and the productivity index increased from 0.88 to 1.37 $t \cdot m^{-2} \cdot h^{-1}$. Meanwhile, the solid fuel consumption decreased from 109.83 to 95.86 $kg \cdot t^{-1}$. When the drying time was further extended to 7 min, the yield continued to increase to 71.67%, and the solid fuel consumption further decreased to 93.91 $kg \cdot t^{-1}$. However, the tumble index and productivity index decreased to 56% and 1.28 $t \cdot m^{-2} \cdot h^{-1}$, respectively. Therefore, although longer drying time was beneficial for increasing yield and reducing fuel consumption, 5 min was more favorable for maintaining tumble strength and sintering productivity.

The influence of drying regime is mainly related to moisture removal, green-pellet stability, and bed permeability before ignition [24]. Insufficient drying temperature or drying time leaves excessive residual moisture in the pellet bed, which increases the heat demand for evaporation during sintering and may cause moisture migration and condensation in the lower bed. This weakens effective heat utilization and slows the downward movement of the combustion front, resulting in lower productivity and higher solid fuel consumption. Increasing the drying intensity within a suitable range promotes moisture removal, improves the thermal state of the pellet bed before ignition, and helps maintain stable gas-flow channels. However, excessive drying may weaken the moisture-mediated bonding within green pellets and reduce their resistance to thermal and mechanical stresses before consolidation, which is unfavorable for maintaining tumble strength and stable sintering. Therefore, a drying temperature of 450 °C and a drying time of 5 min were selected for subsequent pellet-sintering tests.

For the post-ignition holding regime, as shown in Figure 7, increasing the holding temperature from 800 °C to 1000 °C increased the yield from 61.9% to 70.19%, the tumble index increased from 46.53% to 57.87%, and the productivity index increased from 1.08 to 1.37 $t \cdot m^{-2} \cdot h^{-1}$. Meanwhile, the solid fuel consumption decreased from 108.09 to 95.86 $kg \cdot t^{-1}$. When the holding temperature was further increased to 1100 °C, the yield and tumble index continued to increase to 72.4% and 60.27%, respectively, and the solid fuel consumption further decreased to 92.08 $kg \cdot t^{-1}$. However, the productivity index decreased to 1.28 $t \cdot m^{-2} \cdot h^{-1}$. Therefore, although 1100 °C was beneficial for increasing yield and tumble strength, 1000 °C was more favorable for maintaining higher sintering productivity.

The holding time also affected the pellet-sintering performance. With increasing holding time from 6 min to 10 min, the yield increased from 66.95% to 70.19%, and the productivity index increased from 1.13 to 1.37 $t \cdot m^{-2} \cdot h^{-1}$. The tumble index increased from 51.4% to 58.53% when the holding time increased from 6 min to 8 min, and then remained at a relatively high level. Meanwhile, the solid fuel consumption decreased from 100.73 to 95.86 $kg \cdot t^{-1}$ as the holding time increased from 6 min to 10 min. When the holding time was further extended to 12 min, the yield slightly increased to 70.85%, and the solid fuel consumption further decreased to 94.42 $kg \cdot t^{-1}$, but the productivity index decreased to 1.34 $t \cdot m^{-2} \cdot h^{-1}$. Therefore, considering tumble strength, productivity, and fuel consumption, a holding time of 10 min was selected.

The effect of the holding regime is mainly related to post-ignition heat supply, combustion-zone stability, and bonding-phase formation [25]. After ignition, an appropriate holding temperature and holding time can maintain the thermal level of the upper bed, stabilize the combustion zone, and promote heat transfer to the lower bed. This is beneficial for fuel combustion, mineral transformation, and liquid-phase formation, thereby improving yield, tumble strength, and sintering productivity while reducing solid fuel consumption. However, excessive holding temperature or prolonged holding time may broaden the high-temperature zone and increase gas-flow resistance in the pellet bed.

This can slow the effective downward movement of the combustion front and reduce the productivity index, although yield and tumble strength may still be improved. Therefore, a holding temperature of 1000 °C and a holding time of 10 min were selected as suitable post-ignition holding conditions for pellet sintering.

3.5. Selected Pellet-Sintering Conditions, Phase Composition, and Microstructural Characteristics

Based on the above single-factor tests, the selected pellet-sintering conditions for limonitic nickel laterite are summarized in Table 5. Under the fixed basicity of 1.5 and bed height of 850 mm, the selected conditions were determined as follows: moisture content of 21%, solid fuel dosage of 5.8%, return fines dosage of 25%, drying temperature of 450 °C, drying time of 5 min, holding temperature of 1000 °C, and holding time of 10 min. These conditions provided a suitable balance among yield, tumble index, productivity index, and solid fuel consumption within the investigated ranges. Given the sequential single-factor design, possible interactions among the investigated parameters were not evaluated; accordingly, the selected values represent suitable operating conditions within the investigated ranges.

Table 5. Selected pellet-sintering conditions for limonitic nickel laterite.

Parameter	Selected Value
Moisture content, %	21
Solid fuel dosage, %	5.8
Return fines dosage, %	25
Drying temperature, °C	450
Drying time, min	5
Holding temperature, °C	1000
Holding time, min	10

Note: Basicity = 1.5; bed height = 850 mm.

To provide basic characterization of the green pellets used for pellet sintering, representative green pellets prepared under the selected conditions were evaluated in terms of size distribution, compressive strength, and drop strength. The results are summarized in Table 6.

Table 6. Characteristics of green pellets prepared under the selected pelletizing conditions.

Characteristic	Size Fraction, mm, or Test Condition	Value
Size distribution, wt.%	>12	16.23
	10–12	72.31
	8–10	5.47
	5–8	1.70
	3–5	1.76
	<3	2.53
	8–12	77.78
	>5	95.71
Compressive strength, N·pellet^{-1}	—	14.86
Drop strength, drops·pellet^{-1}	Drop height: 0.5 m	≥20

Note: The 8–12 mm and >5 mm fractions are combined values calculated from the original size fractions. Drop strength was determined by repeatedly dropping the green pellets from a height of 0.5 m. The em dash (—) indicates that the corresponding item is not applicable.

As shown in Table 6, the green pellets were predominantly distributed in the 10–12 mm size fraction, which accounted for 72.31 wt.%. The combined proportion of green pellets in the 8–12 mm size range reached 77.78 wt.%, while 95.71 wt.% of the green pellets were larger than 5 mm. In addition, the green pellets exhibited a compressive strength of

14.86 N·pellet^{-1} and a drop strength of at least 20 drops·pellet^{-1} from a height of 0.5 m. These results indicate that the green pellets possessed a concentrated size distribution and sufficient mechanical stability for charging and subsequent pot sintering.

To evaluate the overall strengthening effect of pellet sintering, the sintering performance under pellet sintering was compared with that under conventional sintering, as shown in Table 7. Compared with conventional sintering, pellet sintering increased the yield from 56.58% to 70.19%, the tumble index from 42.69% to 57.87%, and the productivity index from 1.04 to 1.37 t·m^{-2}·h^{-1}. Meanwhile, the solid fuel consumption decreased from 124.28 to 95.86 kg·t^{-1}. Correspondingly, the yield, tumble index, and productivity index increased by 24.05%, 35.56%, and 31.73%, respectively, while the solid fuel consumption decreased by 22.87%.

Table 7. Comparison of sintering performance between conventional sintering and pellet sintering.

Process	Yield, %	Tumble Index, %	Productivity Index, t·m^{-2}·h^{-1}	Solid Fuel Consumption, kg·t^{-1}
Conventional sintering	56.58	42.69	1.04	124.28
Pellet sintering	70.19	57.87	1.37	95.86

The improvement in sintering performance can be mainly attributed to the reconstruction of the pellet-bed structure by pelletizing. Compared with conventional sintering, pellet sintering forms larger and more uniform green pellets, which helps maintain stable inter-pellet voids and improves gas-flow channels in the bed. The improved bed permeability is beneficial for fuel combustion, heat transfer, and the downward movement of the combustion front, thereby increasing the productivity index. In addition, the drying and post-ignition holding treatments reduce the adverse effect of excessive moisture and improve the thermal state of the pellet bed, which favors bonding-phase formation and sinter consolidation. As a result, pellet sintering effectively improved product yield and tumble strength while reducing solid fuel consumption.

The XRD patterns of the conventional sinter and pellet sinter are shown in Figure 8. Both samples exhibited characteristic diffraction peaks of spinel-type phases, indicating that Fe–Mg–Cr–Al-bearing spinels constituted the principal crystalline framework of the sintered products. In the conventional sinter, diffraction peaks associated with 2CaO·SiO_2 were also observed, indicating that calcium silicate was an important bonding phase.

The pellet sinter retained the spinel-rich mineral framework but exhibited a more complex phase assemblage. In addition to the spinel-type phases, diffraction peaks associated with SFCA-type and spinel–olivine composite-bonding-related phases were observed. This indicates that pellet sintering promoted the development of a composite bonding structure involving SFCA-type and spinel–olivine-related phases, rather than a bonding structure dominated mainly by calcium silicate.

To further characterize the pore morphology, local phase distribution, and bonding characteristics, OM and SEM–EDS analyses were performed, as shown in Figure 9. As shown in Figure 9a, the conventional sinter contained many large and irregular pores, and the bonding structure between mineral particles was relatively discontinuous. In contrast, the pellet sinter showed a more compact structure with fewer large pores and a more uniform pore distribution, as shown in Figure 9b. Quantitative image analysis showed that the average two-dimensional pore area fraction decreased from 33.29% in the conventional sinter to 18.05% in the pellet sinter. Meanwhile, the area fraction of large pores with an equivalent diameter greater than 50 μm decreased from 22.25% to 11.61%. These quantitative results indicate that pellet sintering reduced both the overall pore abundance

and the contribution of coarse pores, thereby promoting the formation of a more continuous consolidated structure.

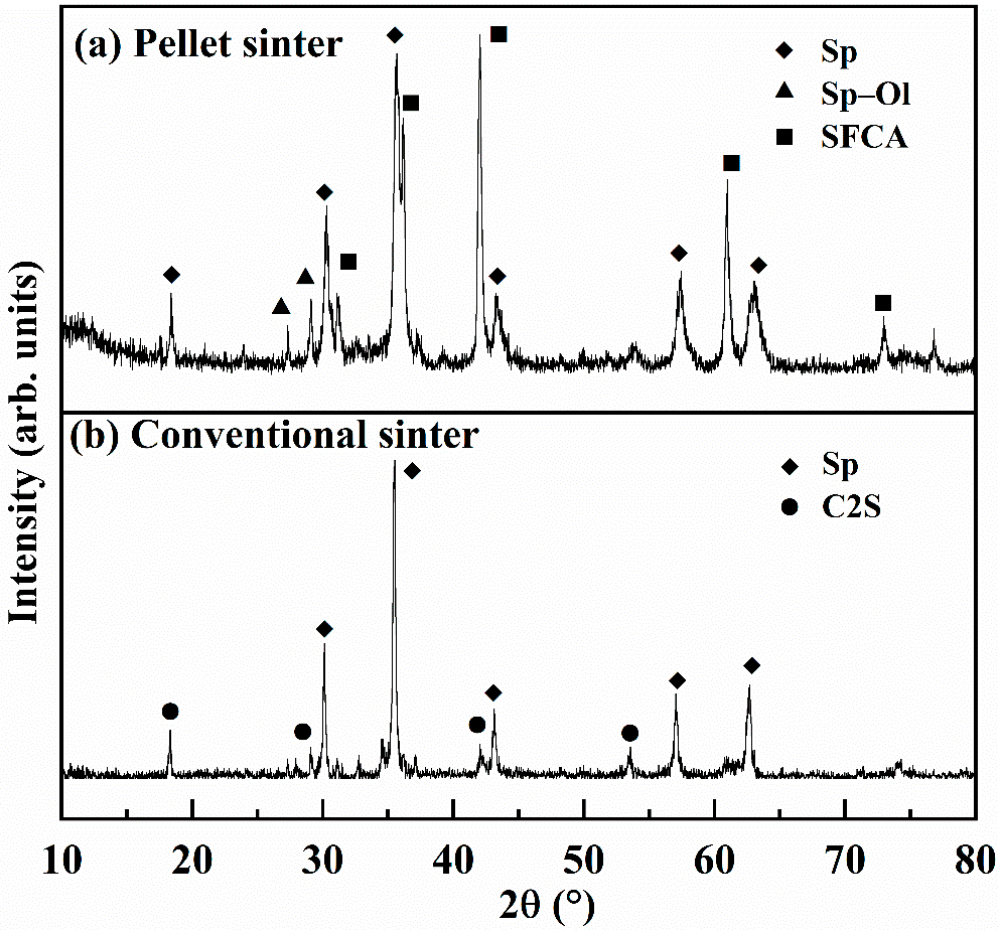


Figure 8. XRD patterns of the pellet sinter and conventional sinter: (**a**) pellet sinter and (**b**) conventional sinter. Sp, spinel-type phases; Sp–Ol, spinel–olivine composite-bonding-related phases; SFCA, silico-ferrite of calcium and aluminum; C2S, $2CaO{\cdot}SiO_2$.

Table 8. EDS analysis results of typical areas in conventional sinter and pellet sinter.

Area No.	Elements (Atomic Conc, %)								Possible Phases
	Fe	Cr	Ni	Mg	Al	Si	Ca	O	
c-1	22.12	14.21	0.36	2.36	2.45	0.12	0.37	58.01	$(Fe,Mg,Ni)(Cr,Al,Fe)_2O_4$
c-2	15.33	15.47	0.32	5.06	5.38	0.01	0.59	57.84	$(Fe,Mg)(Cr,Al,Fe)_2O_4$
c-3	11.48	15.91	0.03	6.45	9.78	0.01	0.06	56.28	$(Mg,Fe)(Cr,Al,Fe)_2O_4$
c-4	27.94	5.44	0.50	1.89	4.75	0.13	0.42	58.93	$(Fe,Mg)(Fe,Al,Cr)_2O_4$
c-5	2.83	0.07	0.01	0.73	4.41	12.73	18.75	60.46	$2CaO{\cdot}SiO_2$
c-6	19.89	19.29	0.32	2.87	1.36	0.01	0.49	55.77	$(Fe,Mg)(Cr,Fe,Al)_2O_4$
d-1	5.09	0.00	0.00	0.60	7.74	8.83	18.70	59.02	$CaO{\cdot}(Fe,Mg)Al_2O_4{\cdot}SiO_2$
d-2	14.54	18.62	0.29	4.07	7.47	0.18	0.30	54.54	$(Mg,Fe)(Cr,Al,Fe)_2O_4$
d-3	16.63	21.98	0.53	1.90	3.27	0.14	0.26	55.28	$(Fe,Mg,Ni)(Cr,Al,Fe)_2O_4$
d-4	20.85	16.94	0.41	2.40	5.99	0.26	0.40	52.76	$(Fe,Mg,Ni)(Cr,Al,Fe)_2O_4$
d-5	2.53	0.01	0.03	0.30	1.79	10.79	26.32	58.23	$2CaO{\cdot}SiO_2$
d-6	5.72	0.00	0.00	0.53	8.89	8.72	18.82	57.33	$CaO{\cdot}(Fe,Mg)Al_2O_4{\cdot}SiO_2$
d-7	22.06	0.02	0.13	0.81	7.61	3.71	8.48	57.19	SFCA

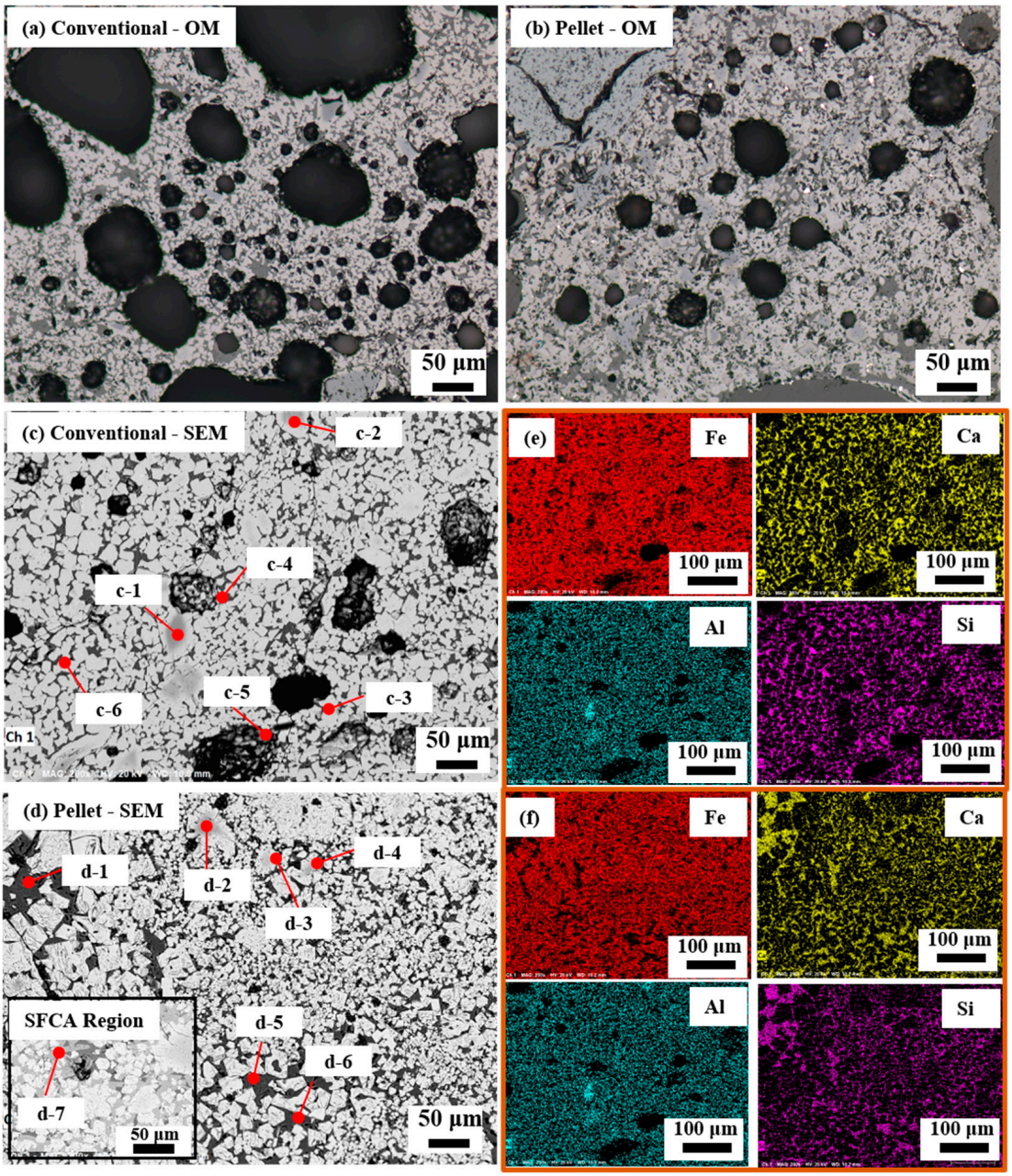


Figure 9. Microstructural characteristics and EDS elemental distributions of the conventional sinter and pellet sinter: (**a**) conventional sinter—OM; (**b**) pellet sinter—OM; (**c**) conventional sinter—SEM; (**d**) pellet sinter—SEM; and (**e**,**f**) corresponding EDS elemental maps of Fe, Ca, Al, and Si acquired from the same fields of view as those shown in (**c**,**d**), respectively. The marked regions in (**c**,**d**) correspond to the point EDS results listed in Table 8. Labels c-1–c-6 and d-1–d-7 indicate the point-EDS analysis locations listed in Table 8; "Ch1" denotes the channel label automatically generated by the EDS mapping software 6.0.

To provide direct visual support for the point EDS results, the corresponding elemental maps acquired from the same fields of view as the SEM images are presented in Figure 9e,f. The Fe, Ca, Al, and Si maps show the spatial distributions of the principal elements in the conventional sinter and pellet sinter and support the compositional differences indicated by the point EDS analyses in Table 8.

The SEM images further reveal the differences in phase distribution and bonding characteristics between the conventional sinter and pellet sinter. As shown in Figure 9c, the conventional sinter was mainly composed of angular mineral particles and locally distributed

bonding phases. The combined XRD and point EDS results indicate that areas c-1, c-2, c-3, c-4, and c-6 were Fe–Cr–Mg–Al-rich spinel-type phases, including $(Fe,Mg,Ni)(Cr,Al,Fe)_2O_4$, $(Mg,Fe)(Cr,Al,Fe)_2O_4$, and $(Fe,Mg)(Cr,Fe,Al)_2O_4$. Area c-5 was characterized by high Ca and Si contents but low Fe content, and was identified as $2CaO{\cdot}SiO_2$, consistent with the calcium-silicate-related diffraction peaks observed in Figure 8b. The elemental maps in Figure 9e further show the spatial distributions of Fe, Ca, Al, and Si within the same field of view. These results indicate that the conventional sinter was dominated by refractory spinel-type phases and calcium silicate, while continuous and effective composite bonding phases were insufficiently developed [26,27].

For the pellet sinter, the SEM image and corresponding elemental maps shown in Figure 9d,f reveal that the mineral particles were more closely connected and that the bonding phases were more continuously distributed between adjacent particles. Based on the combined XRD and point EDS results, areas d-2, d-3, and d-4 were enriched in Fe, Cr, Mg, and Al, and were identified as spinel-type phases, such as $(Mg,Fe)(Cr,Al,Fe)_2O_4$ and $(Fe,Mg,Ni)(Cr,Al,Fe)_2O_4$. These spinel-type phases constituted an important mineral framework in the pellet sinter. Area d-5 was rich in Ca and Si and was identified as $2CaO{\cdot}SiO_2$, indicating that a small amount of calcium silicate remained locally. In contrast, areas d-1 and d-6 contained high Ca, Si, and Al contents, together with certain Fe and Mg contents, and were compositionally consistent with $CaO{\cdot}(Fe,Mg)Al_2O_4{\cdot}SiO_2$. Combined with the Sp–Ol-related diffraction features shown in Figure 8a, these regions were interpreted as spinel–olivine eutectic-type composite bonding phases. In addition, the inset in Figure 9d shows an SFCA-rich region in the pellet sinter. The EDS result of area d-7 showed simultaneous enrichment of Fe, Ca, Al, and Si, and the corresponding SFCA-related diffraction peaks in Figure 8a further support its identification as an SFCA-rich bonding region [28]. The elemental maps in Figure 9f show the corresponding spatial distributions of Fe, Ca, Al, and Si within the same field of view.

From a thermodynamic perspective, the interpretation of the Ca–Fe–Mg–Al–Si-rich regions as spinel–olivine eutectic-type composite bonding phases is consistent with the phase-equilibrium relationships reported for relevant oxide subsystems. Thermodynamic optimization of the Al_2O_3–FeO–Fe_2O_3–SiO_2 system indicates that the stability and coexistence of oxide solid phases and liquid are strongly controlled by temperature, bulk composition, and oxygen partial pressure [29]. Experimental phase-equilibrium studies of the FeO–Fe_2O_3–MgO–SiO_2 system in air further demonstrate the existence of liquid, spinel, and olivine primary-phase fields and the coexistence of these phases under high-temperature conditions [30]. Although these subsystem studies do not fully reproduce the multicomponent Ca–Fe–Mg–Al–Si–Cr–O composition of the present sinter, they provide thermodynamic support for the coexistence of spinel- and olivine-type constituents with a liquid-derived bonding phase during high-temperature sintering and subsequent cooling.

The identification of area d-7 as an SFCA-rich bonding region is also consistent with the reported formation and stability relationships of SFCA-type phases. In situ synchrotron X-ray diffraction studies have shown that SFCA and SFCA-I can form during heating and undergo further crystallization or transformation during subsequent cooling [31]. Thermochemical investigations further demonstrate the thermodynamic stability of SFCA and SFCA-I phases and relate this stability to their complex, compositionally disordered crystal structures [32]. These findings provide additional thermodynamic support for the SFCA-type phase identified in the pellet sinter.

Overall, the pellet sinter was characterized by a spinel-rich mineral framework, with a small amount of calcium silicate locally remaining. More importantly, pellet sintering promoted the formation of spinel–olivine eutectic-type composite bonding phases and SFCA-type bonding phases. These effective bonding phases filled the inter-particle re-

gions and connected the spinel-type particles and other mineral phases more continuously, resulting in a more compact and integrated consolidation structure [27,33]. Therefore, pellet sintering changed the consolidation behavior from discontinuous local bonding to a more continuous composite-bonding structure. This structural reconstruction demonstrates that pellet sintering is a feasible route for strengthening sinter consolidation and promoting the efficient utilization of limonitic nickel laterite. The improved strength and integrated bonding structure make the pellet sinter produced from limonitic nickel laterite suitable as an Fe–Ni–Cr-bearing burden for subsequent reduction and smelting in stainless-steel production.

4. Conclusions

In this study, pellet sintering was proposed as a process-intensification route for improving the sintering performance of limonitic nickel laterite. By evaluating the effects of key pellet-sintering parameters and identifying suitable operating conditions, this work provides a feasible approach for strengthening sinter consolidation and promoting the efficient utilization of limonitic nickel laterite. The main conclusions are as follows:

1. The suitable pellet sintering conditions were determined as follows: moisture content of 21%, solid fuel dosage of 5.8%, return fines dosage of 25%, drying temperature of 450 °C, drying time of 5 min, holding temperature of 1000 °C, and holding time of 10 min, under a fixed basicity of 1.5 and a bed height of 850 mm. These conditions provided a suitable balance among green-pellet stability, bed permeability, heat supply, and sinter consolidation.
2. Under the above pellet sintering conditions, the yield, tumble index, productivity index, and solid fuel consumption reached 70.19%, 57.87%, 1.37 $t \cdot m^{-2} \cdot h^{-1}$, and 95.86 $kg \cdot t^{-1}$, respectively. Compared with conventional sintering, pellet sintering increased the yield, tumble index, and productivity index by 24.05%, 35.56%, and 31.73%, respectively, while reducing the solid fuel consumption by 22.87%. This indicates that pellet sintering effectively improved product quality and sintering productivity while reducing solid fuel consumption within the defined calculation boundary.
3. Combined XRD, OM, quantitative image analysis, and SEM–EDS results showed that the conventional sinter contained large irregular pores and discontinuous bonding structures and was dominated by spinel-type phases and $2CaO \cdot SiO_2$. Pellet sintering reduced the average two-dimensional pore area fraction from 33.29% to 18.05% and the large-pore area fraction from 22.25% to 11.61%, resulting in a more compact and continuous consolidation structure. On the basis of the spinel-rich mineral framework, pellet sintering promoted the formation of spinel–olivine eutectic-type composite bonding phases and SFCA-type bonding phases, while only a small amount of calcium silicate remained locally. These effective bonding phases strengthened the connection between mineral particles and contributed to the formation of a compact and continuous consolidation structure, thereby improving the overall sintering performance of limonitic nickel laterite.

Author Contributions: Conceptualization, G.L., D.Z. and J.P.; methodology, G.L., J.P. and W.L.; investigation, data curation, formal analysis, visualization, and writing—original draft preparation, G.L.; resources, D.Z., J.P., Q.S. and M.W.; writing—review and editing, D.Z., J.P., Q.S., W.L. and M.W.; supervision, D.Z., J.P. and W.L.; funding acquisition, J.P. All authors have read and agreed to the published version of the manuscript.

Funding: This research was funded by the National Key Research and Development Program of China, grant numbers 2023YFC3903900 and 2023YFC3903904.

Data Availability Statement: The raw data supporting the conclusions of this article will be made available by the authors on request.

Acknowledgments: The authors acknowledge the support of the Vale-CSU Joint Laboratory for Low-Carbon and Hydrogen Metallurgy, Central South University.

Conflicts of Interest: Author Ming Wang was employed by Quzhou Huayou Resource Recycling Technology Co., Ltd. The remaining authors declare no conflicts of interest.

References

1. Butt, C.R.M.; Cluzel, D. Nickel Laterite Ore Deposits: Weathered Serpentinites. *Elements* **2013**, *9*, 123–128. [CrossRef]
2. Oxley, A.; Barcza, N. Hydro–Pyro Integration in the Processing of Nickel Laterites. *Miner. Eng.* **2013**, *54*, 2–13. [CrossRef]
3. Guo, E.; Liu, M.; Pan, C.; Yuan, Q.; Lv, X. Sintering Process for Limonitic Nickel Laterite. In *Proceedings of the Celebrating the Megascale*; Mackey, P.J., Grimsey, E.J., Jones, R.T., Brooks, G.A., Eds.; Springer International Publishing: Cham, Switzerland, 2016; pp. 623–630.
4. Zhu, D.; Xue, Y.; Pan, J.; Yang, C.; Guo, Z.; Tian, H.; Liao, H.; Pan, L.; Huang, X. An Investigation into the Distinctive Sintering Performance and Consolidation Mechanism of Limonitic Laterite Ore. *Powder Technol.* **2020**, *367*, 616–631. [CrossRef]
5. Xue, Y.; Zhu, D.; Pan, J.; Guo, Z.; Tian, H.; Wang, D.; Pan, L. Distinct Difference in High-Temperature Characteristics between Limonitic Nickel Laterite and Ordinary Limonite. *ISIJ Int.* **2022**, *62*, 29–37. [CrossRef]
6. Xue, Y.; Zhu, D.; Pan, J.; Guo, Z.; Tian, H.; Li, G.; Huang, Q.; Pan, L.; Huang, X. Significant Influence of Self-Possessed Moisture of Limonitic Nickel Laterite on Sintering Performance and Its Action Mechanism. *J. Iron Steel Res. Int.* **2022**, *29*, 1368–1380. [CrossRef]
7. Tu, Y.; Zhang, Y.; Su, Z.; Jiang, T. Mineralization Mechanism of Limonitic Laterite Sinter under Different Fuel Dosage: Effect of FeO. *Powder Technol.* **2022**, *398*, 117064. [CrossRef]
8. Xue, Y.; Zhu, D.; Pan, J.; Guo, Z.; Yang, C.; Tian, H.; Huang, Q.; Pan, L.; Huang, X. An Investigation into the Co-Sintering Process of Limonitic Nickel Laterite and Low-Grade Chromite via Multi-Force Fields. *J. Mater. Res. Technol.* **2021**, *12*, 1816–1831. [CrossRef]
9. Xue, Y.; Zhu, D.; Pan, J.; Li, G.; Lv, X. Reduction of Carbon Footprint Through Hybrid Sintering of Low-Grade Limonitic Nickel Laterite and Chromite Ore. *J. Sustain. Metall.* **2023**, *9*, 648–664. [CrossRef]
10. Niu, L.; Zhang, J.; Wang, Y.; Kang, J.; Li, S.; Shan, C.; Li, Z.; Liu, Z. Iron Ore Granulation for Sinter Production: Developments, Progress, and Challenges. *ISIJ Int.* **2023**, *63*, 601–612. [CrossRef]
11. Yamaguchi, Y.; Kamijo, C.; Matsumura, M.; Kawaguchi, T. Improvement of Permeability of Sintering Bed by Adding Dry Particles to Granulated Raw Materials. *ISIJ Int.* **2013**, *53*, 1538–1544. [CrossRef]
12. Oliveira, V.D.M.; Domingues, A.L.A.; Bagatini, M.C.; Resende, V.G.D. Granulation Behavior of an Iron Ore Sintering Mixture Containing High Grade Pellet Feed with Different Specific Surface. *ISIJ Int.* **2020**, *60*, 2376–2384. [CrossRef]
13. Iveson, S.M.; Holt, S.; Biggs, S. Advancing Contact Angle of Iron Ores as a Function of Their Hematite and Goethite Content: Implications for Pelletising and Sintering. *Int. J. Miner. Process.* **2004**, *74*, 281–287. [CrossRef]
14. Tang, K.; Lv, X.; Wu, S.; Xuan, S.; Huang, X.; Bai, C. Measurement for Contact Angle of Iron Ore Particles and Water. *ISIJ Int.* **2018**, *58*, 379–400. [CrossRef]
15. Zhou, H.; Lai, Z.; Lv, L.; Fang, H.; Meng, H.; Zhou, M.; Cen, K. Improvement in the Permeability of Sintering Beds by Drying Treatment after Granulating Sinter Raw Materials Containing Concentrates. *Adv. Powder Technol.* **2020**, *31*, 3297–3306. [CrossRef]
16. Fernández-González, D.; Piñuela-Noval, J.; FelipeVerdeja, L. Iron Ore Agglomeration Technologies. In *Iron Ores and Iron Oxide Materials*; IntechOpen: London, UK, 2017; ISBN 978-1-78923-321-6.
17. Lv, X.; Bai, C.; He, S.; Huang, Q. Mineral Change of Philippine and Indonesia Nickel Lateritic Ore during Sintering and Mineralogy of Their Sinter. *ISIJ Int.* **2010**, *50*, 380–385. [CrossRef]
18. Wu, S.; Zhu, J.; Bei, J.; Zhang, G.; Zhai, X. Effects of Particle Characteristics on the Granulation Ability of Iron Ores during the Sintering Process. *Int. J. Miner. Metall. Mater.* **2015**, *22*, 907–916. [CrossRef]
19. *ISO 3271:2015*; Iron Ores for Blast Furnace and Direct Reduction Feedstocks—Determination of the Tumble and Abrasion Indices. International Organization for Standardization: Geneva, Switzerland, 2015.
20. Zhou, H.; Meng, H.; Ma, P.; Wang, J.; Cheng, F.; Fang, H. Experimental Investigation on the Effect of Granulation Moisture on the Flame Front Propagation and Pore Structure in the High-Temperature Zone of the Sinter Bed. *Powder Technol.* **2022**, *396*, 663–672. [CrossRef]
21. Zhou, M.; Xu, J.; Zhou, H. Evaluating the Permeability Properties of Green Bed in Iron Ore Sintering Using High Resolution X-Ray Computed Tomography and Orthogonal Array Tests. *Powder Technol.* **2020**, *375*, 360–368. [CrossRef]
22. Tomas Da Rocha, L.; Cho, S.; Kim, S.-W.; Jung, S.-M. Effects of Adding Iron Ores-Based Calcium Ferrites to the Sinter Mix on Sinter Quality and Reduction of CO_2, NO and SO_2. *ISIJ Int.* **2022**, *62*, 2587–2598. [CrossRef]

23. Sun, C.; Ma, P.; Deng, J.; Bai, L.; Liao, Z.; Pei, Y.; Zhang, Q.; Xu, J. Intensive Reduction of Fuel Consumption in the Sintering Process of Double-Layered Fuel Segregation with Return Fines Embedding. *Fuel* **2023**, *332*, 125955. [CrossRef]
24. Matsumura, M.; Yamaguchi, Y.; Hara, M.; Kamijo, C.; Kawaguchi, T. Effect of Drying Treatment after Granulating Sinter Raw Materials on Flame Front Speed and Sintering Yield. *ISIJ Int.* **2018**, *58*, 1013–1021. [CrossRef]
25. Wu, S.; Li, H.; Zhang, W.; Su, B. Effect of Thermodynamic Melt Formation Characteristics on Liquid Phase Fluidity of Iron Ore in the Sintering Process. *Metals* **2019**, *9*, 404. [CrossRef]
26. Li, G.; Zhi, Q.; Rao, M.; Zhang, Y.; Cai, W.; Jiang, T. Effect of Basicity on Sintering Behavior of Saprolitic Nickel Laterite in Air. *Powder Technol.* **2013**, *249*, 212–219. [CrossRef]
27. Loo, C.E.; Leung, W. Factors Influencing the Bonding Phase Structure of Iron Ore Sinters. *ISIJ Int.* **2003**, *43*, 1393–1402. [CrossRef]
28. Nicol, S.; Chen, J.; Pownceby, M.I.; Webster, N.A.S. A Review of the Chemistry, Structure and Formation Conditions of Silico-Ferrite of Calcium and Aluminum ('SFCA') Phases. *ISIJ Int.* **2018**, *58*, 2157–2172. [CrossRef]
29. Prostakova, V.; Shishin, D.; Shevchenko, M.; Jak, E. Thermodynamic Optimization of the Al2O3–FeO–Fe2O3–SiO2 Oxide System. *Calphad* **2019**, *67*, 101680. [CrossRef]
30. Babaian, I.; Shevchenko, M.; Nekhoroshev, E.; Jak, E. Integrated Experimental Phase Equilibria and Thermodynamic Modelling Investigation of the FeO–Fe2O3–MgO and the FeO–Fe2O3–MgO–SiO2 Systems. Part I: Experimental Results in Air. *ISIJ Int.* **2024**, *64*, 2087–2097. [CrossRef]
31. Webster, N.A.S.; Pownceby, M.I.; Madsen, I.C.; Kimpton, J.A. Silico-Ferrite of Calcium and Aluminum (SFCA) Iron Ore Sinter Bonding Phases: New Insights into Their Formation During Heating and Cooling. *Metall. Mater. Trans. B* **2012**, *43*, 1344–1357. [CrossRef]
32. Koryttseva, A.; Webster, N.A.S.; Pownceby, M.I.; Navrotsky, A. Thermodynamic Stability of SFCA (Silico-ferrite of Calcium and Aluminum) and SFCA-I Phases. *J. AM. Ceram. Soc.* **2017**, *100*, 3646–3651. [CrossRef]
33. Zhou, M.; Zhou, H. Experimental Investigation and Numerical Modeling of Strength Properties of Iron Ore Sinter Based on Pilot-Scale Pot Tests and X-Ray Computed Tomography. *J. Mater. Res. Technol.* **2020**, *9*, 13106–13117. [CrossRef]

Disclaimer/Publisher's Note: The statements, opinions and data contained in all publications are solely those of the individual author(s) and contributor(s) and not of MDPI and/or the editor(s). MDPI and/or the editor(s) disclaim responsibility for any injury to people or property resulting from any ideas, methods, instructions or products referred to in the content.